This is a copy of the published version, or version of record, available on the publisher's website. This version does not track changes, errata, or withdrawals on the publisher's site.

One-dimensional quantum magnetism in the S = 1/2 Mo(V) system KMoOP2O7

Aly H. Abdeldaim, Alexander A. Tsirlin, Jacques Ollivier, Clemens Ritter, Dominic Fortes, Robin S. Perry, Lucy Clark, and Gøran J. Nilsen

Published version information

Citation: AH Abdeldaim et al. One-dimensional quantum magnetism in the S = 1/2 Mo(V) system KMoOP2O7. Phys Rev B 107, no. 1 (2023): 014415

DOI: 10.1103/PhysRevB.107.014415

This version is made available in accordance with publisher policies. Please cite only the published version using the reference above. This is the citation assigned by the publisher at the time of issuing the APV. Please check the publisher's website for any updates.

This item was retrieved from **ePubs**, the Open Access archive of the Science and Technology Facilities Council, UK. Please contact epublications@stfc.ac.uk or go to http://epubs.stfc.ac.uk/ for further information and policies.

One-dimensional quantum magnetism in the $S = \frac{1}{2}$ Mo(V) system $KMoOP_2O_7$

Aly H. Abdeldaim,[1,2,*] Alexander A. Tsirlin,[3] Jacques Ollivier,[4] Clemens Ritter,[4] Dominic Fortes,[2] Robin S. Perry,[5,2] Lucy Clark,[1] and Gøran J. Nilsen[2,6,†]

[1]*School of Chemistry, University of Birmingham, Edgbaston, Birmingham B15 2TT, United Kingdom*
[2]*ISIS Neutron and Muon Source, Science and Technology Facilities Council, Didcot OX11 0QX, United Kingdom*
[3]*Felix Bloch Institute for Solid-State Physics, Leipzig University, 04103 Leipzig, Germany*
[4]*Institut Laue-Langevin, 71 Avenue des Martyrs, CS20156, 38042 Grenoble Cédex 9, France*
[5]*London Centre for Nanotechnology and Department of Physics and Astronomy, University College London, London WC1E 6BT, United Kingdom*
[6]*Department of Mathematics and Physics, University of Stavanger, 4036 Stavanger, Norway*

(Received 4 July 2022; revised 14 November 2022; accepted 12 December 2022; published 19 January 2023)

We present a comprehensive experimental and *ab initio* study of the $S = 1/2$ Mo^{5+} system, $KMoOP_2O_7$, and show that it realizes the $S = \frac{1}{2}$ Heisenberg chain antiferromagnet model. Powder neutron diffraction reveals that $KMoOP_2O_7$ forms a magnetic network comprised of pairs of Mo^{5+} chains within its monoclinic $P2_1/n$ structure. Antiferromagnetic interactions within the Mo^{5+} chains are identified through magnetometry measurements and confirmed by analysis of the magnetic specific heat. The latter reveals a broad feature centered on $T_N = 0.54$ K, which we ascribe to the onset of long-range antiferromagnetic order. No magnetic Bragg scattering is observed in powder neutron-diffraction data collected at 0.05 K, however, which is consistent with a strongly suppressed ordered moment with an upper limit $\mu_{ord} < 0.15\ \mu_B$. The one-dimensional character of the magnetic correlations in $KMoOP_2O_7$ is verified through analysis of inelastic neutron-scattering data, resulting in a model with $J_2 \approx 34$ K and $J_1 \approx -2$ K for the intrachain and interchain exchange interactions, respectively. The origin of these experimental findings are addressed through density-functional theory calculations.

DOI: 10.1103/PhysRevB.107.014415

I. INTRODUCTION

The relevance of the dynamical properties of fractionalized states of matter to fault-tolerant quantum computing [1–3] demands the realization of such quantum states in strongly correlated electron systems [4]. This interest is complemented by the need to develop a fundamental understanding of fractionalized states in condensed-matter systems, such as certain quantum spin liquid models, that host fractionalized quasiparticle excitations [4–6]. The broad interest in the field is highlighted by recent theoretical and experimental investigations of the emergent fractional quasiparticles of spin models hosting, to name a few, monopoles [7], Majorana fermions [8], and the fractional quantum Hall effect[9].

In this vein, owing to the exact solvability of its spin Hamiltonian [10,11], the $S = \frac{1}{2}$ Heisenberg chain antiferromagnet model (HAF) offers a canonical platform for the direct observation of fractional excitations. Known as spinons, the elementary excitations of the HAF manifest as continua as observed in the landmark neutron-scattering studies of $KCuF_3$ [12] and $CuSO_4 \cdot 5H_2O$ [13]. More recently, focus has shifted towards investigating the ground states arising from the perturbative effects of spin-orbit coupling, applied magnetic fields, and frustration to the HAF model [14–16]. A less explored model in this context is the frustrated $S = \frac{1}{2}$ Heisenberg chain model (FCM), which provides a rich magnetic phase diagram dependent on the degree of frustration, $\alpha = J_1/J_2$, between the linear intrachain, J_2, and interchain, J_1, exchange interactions. Although a spontaneous dimer-fluid ground state has been predicted for $\alpha > 0.241$ [17–19], only a few experimental realizations have been identified for the FCM model [20–23], and the presence of the spin gap associated with the dimerization has yet to be conclusively observed.

Motivated by the richness of the exotic phases predicted for this model, we have explored the Mo^{5+} pyrophosphate family of materials, $AMoOP_2O_7$ (A = Na–Cs) [24–27], whose structures form pairs of chains of $4d^1$ Mo^{5+} ions (Fig. 1) that could be amenable to frustration. To this end, we here investigate the structural and magnetic properties of $KMoOP_2O_7$ (Fig. 1) and show that it falls on the Heisenberg one-dimensional limit of the $S = \frac{1}{2}$ HAF model. We begin by reporting our experimental and *ab initio* methodology in Sec. II. Using neutron powder diffraction, we verify the previously published monoclinic structure [24] at room temperature and present its temperature dependence down to 50 mK (Sec. III A). The one-dimensional magnetic behavior of the system is then explored through thermodynamic-property measurements and neutron powder diffraction (NPD) (Secs. III B–III D). Following this, the one-dimensional character of the magnetic correlations in $KMoOP_2O_7$ is discussed through the lens of its electronic structure in Sec. III E. We finally estimate the parameters of the Hamiltonian using inelastic neutron scattering (INS) in Sec. III F before concluding in Sec. IV.

*axa1699@student.bham.ac.uk
†goran.nilsen@stfc.ac.uk

 ©2023 American Physical Society

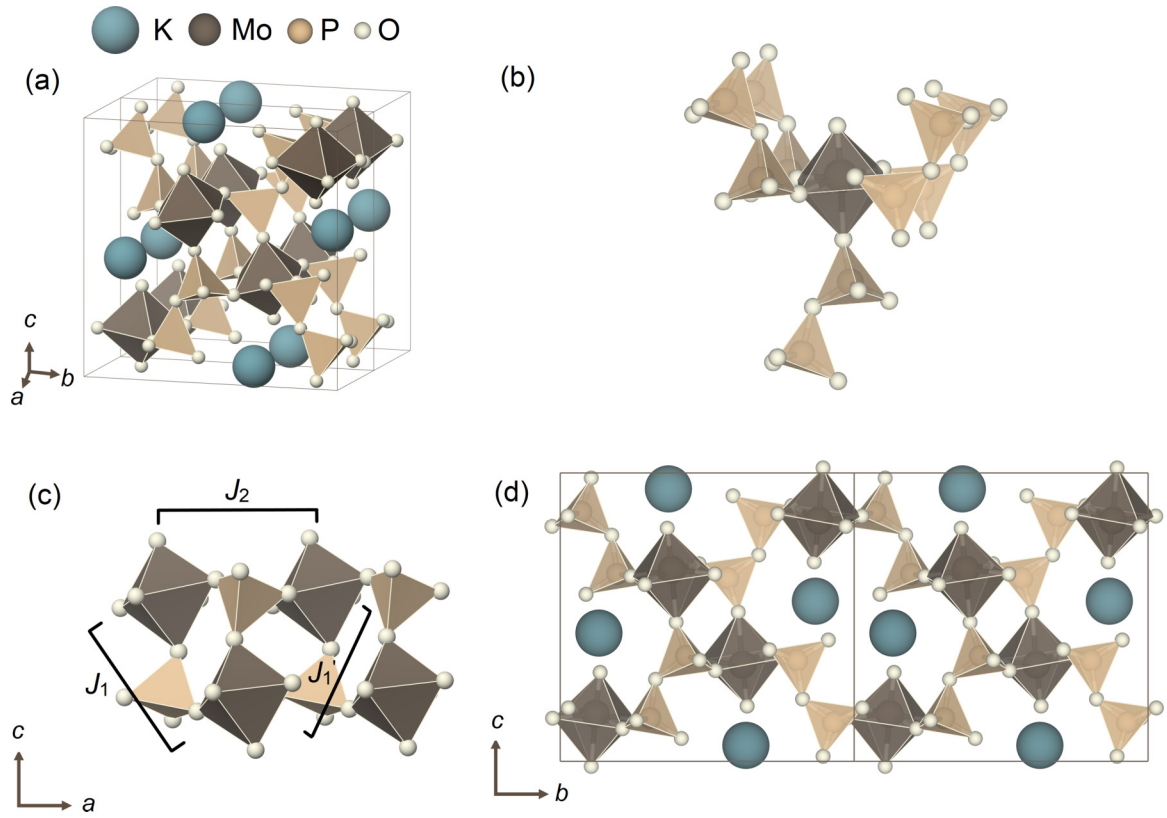

FIG. 1. (a) $P2_1/n$ crystal structure of $KMoOP_2O_7$ as viewed along the [111] direction. (b) The Mo^{5+} ions are situated within a distorted octahedral environment and are bridged by $[PO_4]^{3-}$ tetrahedra along the crystallographic a axis to form (c) a quasi-one-dimensional network of pairs of Mo(V) chains with possible intrachain, J_2, and interchain, J_1 and J_1', superexchange Mo-O-P-O-Mo interaction pathways. (d) This forms a tunnel structure along the crystallographic a axis where the K^+ ions lie. The figure was generated using the VESTA visualization software [28].

II. METHODS

Polycrystalline samples of $KMoOP_2O_7$ were prepared following a modified version of a previously published method [24]. MoO_3 (Alfa Aesar, 99.998%), Mo (powder, <150 μm, 99.9%) $(NH_4)_2HPO_4$ (Alfa Aesar, 98%+), and K_2CO_3 (Sigma Aldrich, 99.995%) were combined in the molar ratio 1.72 : 0.28 : 4 : 1 and intimately ground in a planetary ball mill for 30 minutes in an isopropanol medium and then pressed into a pellet. Samples were sintered in an alumina crucible at 773 K for 24 hours before being reground and pelletized for a second heating stage at 973 K for 24 hours, which resulted in a green-colored product. A 5 g sample of this product was used in all of the following experiments. The synthesis of the isostructural diamagnetic analog, $KNbOP_2O_7$, is described in the Supplemental Material [29].

Powder neutron-diffraction experiments were carried out in 10 K steps between 300 and 200 K on the high-resolution powder diffractometer (HRPD) at the ISIS Neutron and Muon Source. To probe the possible presence of magnetic scattering, powder neutron-diffraction experiments were also performed on the D20 diffractometer [30] at the Institut Laue-Langevin (ILL) and on the WISH diffractometer at the ISIS Neutron and Muon Source. Two data sets were collected on each instrument at 1.8 and 0.05 K and 20 and 1.8 K, respectively. The structural model was refined using the Rietveld method applied in the GSAS software package [31]. Magnetic structure analysis was conducted using the MAG2POL software package [32]. Similar to the approach taken for other Mo^{5+}-containing materials [33], we use an averaged Cr^{4+} and W^{5+} magnetic form factor to approximate that of Mo^{5+}.

Temperature-dependent DC magnetic susceptibility data were measured on a Quantum Design MPMS3 SQUID magnetometer between 1.8 and 300 K using a 22.25 mg sample. Measurements were performed using both zero-field- and field-cooled protocols in an applied magnetic field of 1000 Oe. As no splitting between the zero-field- and field-cooled curves was observed, only the zero-field-cooled measurement is shown here. Calculations for the exact diagonalization of the Heisenberg frustrated chain model were performed using the ALPS software package on a chain of $L = 18$ spins. The resulting model was fit to the experimental data using nonlinear least squares regression, where the only fitting parameter was the intrachain exchange interaction J_2. The interchain coupling J_1 was varied in $0.01J_2$ steps between $-0.3J_2$ and $0.3J_2$.

Specific-heat measurements were performed on a 5.58 mg sample on a Quantum Design PPMS measurement system between 1.8 and 300 K. A lower-temperature measurement, between 0.1 and 4 K, was performed using a dilution refrigeration insert.

The dynamical structure factor, $S(Q, E = \hbar\omega)$, was measured on the direct geometry time-of-flight spectrometer IN5 at the ILL [34]. An incident energy of $E_i = 14.2$ meV (2.4 Å) was used to collect data at 1.8 K for both $KMoOP_2O_7$ and its

isostructural diamagnetic analog, $KNbOP_2O_7$. The exact expression for the two- and four-spinon continuum, $S(Q,E)^{\rm calc}_{2+4}$, was obtained from the exact expression of Caux and Hagemans [35]. To determine the powder-averaged $S(Q,E)^{\rm calc}_{2+4}$, a uniform cross section of the constant-Q sphere was obtained by normalizing random coordinates generated by a Gaussian distribution to the sphere radius. The effect of the interchain exchange interaction J_1, on the other hand, was calculated using the random-phase approximation (RPA) style approach developed by Kohno *et al.* [36]. Fitting the experimental dynamical structure factor using this model was done using a particle swarm optimization algorithm. Here, the fitting parameters were constant across all four cuts used and were the intra- and interchain exchange parameters J_2 and J_1, an amplitude, and a background term.

Interaction parameters of the spin Hamiltonian

$$\mathcal{H} = \sum_{\langle ij \rangle} J_{ij} S_i S_j, \tag{1}$$

where the summation is over lattice bonds ⟨ij⟩, were obtained from density-functional theory (DFT) band-structure calculations performed in the FPLO [37] code using the generalized gradient approximation (GGA) for the exchange-correlation potential [38]. A dense k mesh with up to 152 points in the symmetry-irreducible part of the Brillouin zone for the crystallographic unit cell and 64 points in the doubled supercell were used. All calculations were performed in the full-relativistic mode for the experimental crystal structure of $KMoOP_2O_7$ determined in this work.

The exchange parameters $J_{\rm ij}$ were extracted using two complementary approaches. In the first, we calculated hopping integrals between the Mo 4d states using Wannier functions constructed for the uncorrelated (GGA) band structure, and introduced these hoppings into the Kugel-Khomskii model that leads to the magnetic exchange couplings as follows [39,40]:

$$J_{\rm ij} = \frac{4\left[t_{\rm ij}^{(nn)}\right]^2}{U_{\rm eff}} - \sum_m \frac{4\left[t_{\rm ij}^{(nm)}\right]^2 J_{\rm eff}}{(U_{\rm eff}+\Delta_{\rm m})(U_{\rm eff}-J_{\rm eff}+\Delta_{\rm m})}, \tag{2}$$

where the first and second terms represent antiferromagnetic and ferromagnetic contributions, respectively. Here, $U_{\rm eff} = 4$ eV is the effective on-site Coulomb repulsion and $J_{\rm eff} = 0.5$ eV is the effective Hund's coupling in the Mo 4d shell. The hoppings $t_{\rm ij}^{(\rm nn)}$ are between the half filled states of Mo, whereas $t_{\rm ij}^{(\rm nm)}$ involve the higher-lying empty states m, and $\Delta_{\rm m} = \epsilon_{\rm m} - \epsilon_{\rm n}$ is the crystal-field splitting. In the second approach, we obtained the exchange couplings by a mapping procedure [41,42] using total energies of collinear spin configurations evaluated within DFT + U, where correlation effects in the Mo 4d shell are treated on a mean-field level with the on-site Coulomb repulsion $U_{\rm d} = 4$ eV, Hund's coupling, $J_{\rm d} = 0.5$ eV, and atomic-limit flavor of the double-counting correction. This set of parameters gave the best agreement with the experimental results for the leading exchange coupling, although the corresponding $\tilde{U} = U_{\rm d} - J_{\rm d} = 3.5$ eV is somewhat higher than the 2.0–2.5 eV used in previous studies [43–45]. The DFT + U calculations were performed for the supercell doubled along the a axis due to strong antiferromagnetic interactions along this direction.

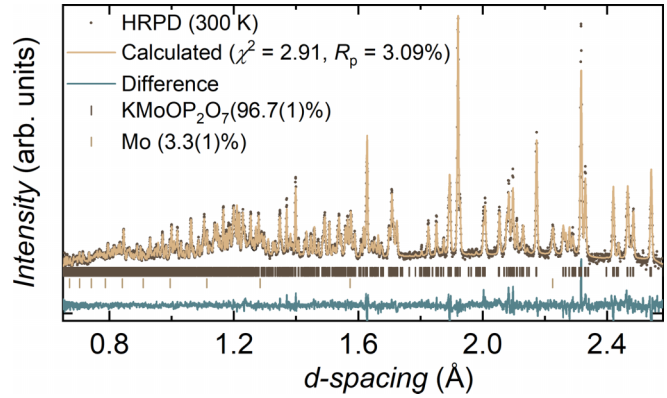

FIG. 2. Rietveld refinement of the $P2_1/n$ model to neutron powder diffraction data collected at 300 K on the HRPD instrument at the ISIS Neutron and Muon Source with goodness-of-fit parameters $\chi^2 = 2.91$ and $R_{\rm p} = 3.09\%$ and the structural model $a = 5.0842(1)$ Å, $b = 11.7243(2)$ Å, $c = 11.5077(2)$ Å, $\beta = 90.975(1)^\circ$.

III. RESULTS

A. Crystal structure

Through a Rietveld analysis of NPD data, the $P2_1/n$ model [24] was confirmed to describe the crystal structure of $KMoOP_2O_7$ at all measured temperatures down to 50 mK. A representative Rietveld refinement ($\chi^2 = 2.91$, $R_{\rm p} = 3.09\%$) of data collected at 300 K, which results in the model described in Table S.1 of the Supplemental Material [29], is shown in Fig. 2. Analysis of data collected at different temperatures is shown in Fig. S2 of the Supplemental Material [29]. The resulting crystal structure [Fig. 1(a)] can be described as a network of octahedrally coordinated Mo^{5+} ions [Fig. 1(b)] that propagate along the crystallographic a axis through $[PO_4]^{3-}$ tetrahedral bridges to form Mo^{5+}-containing chains. Each Mo-octahedron is coordinated by five P_2O_7 groups which leave a short apical bond, connected to a K cation, that distorts the octahedral geometry [Fig. 1(c)]. This forms a tunnel like cavity, occupied by K cations, that lie along the crystallographic a axis [Fig. 1(d)]. The relevant nearest-neighbor superexchange interactions are most likely to be mediated by the Mo-O-P-O-Mo pathways within and between the pairs of chains. Following the nomenclature of the Heisenberg frustrated chain model, those interactions can be described by the intrachain, J_2, and interchain, J_1 and J_1', superexchange parameters with Mo-Mo distances of 5.09(1), 5.36(1), and 5.40(1) Å, respectively [Fig. 1(c)]. These pairs of chains are separated from others within the bc plane by pyrophosphate molecules with distances ranging 6.18(1)–6.94(1) Å. Similar to other Mo^{5+} and V^{4+} containing materials [25,46,47], the formation of a short apical bond distorts the octahedral geometry with apical bond distances of $d_{\rm Mo-O7} = 1.67(1)$ Å and $d_{\rm Mo-O1} = 2.14(1)$ Å.

B. Magnetometry

The temperature dependence of the zero-field-cooled molar magnetic susceptibility is shown in Fig. 3(a). Between 160 and 300 K, $\chi_{\rm m}$ is well described by the modified Curie-Weiss (CW) law, $\chi_{\rm m}(T) = C/(T - \theta_{\rm CW}) + \chi_0$, where $C =$

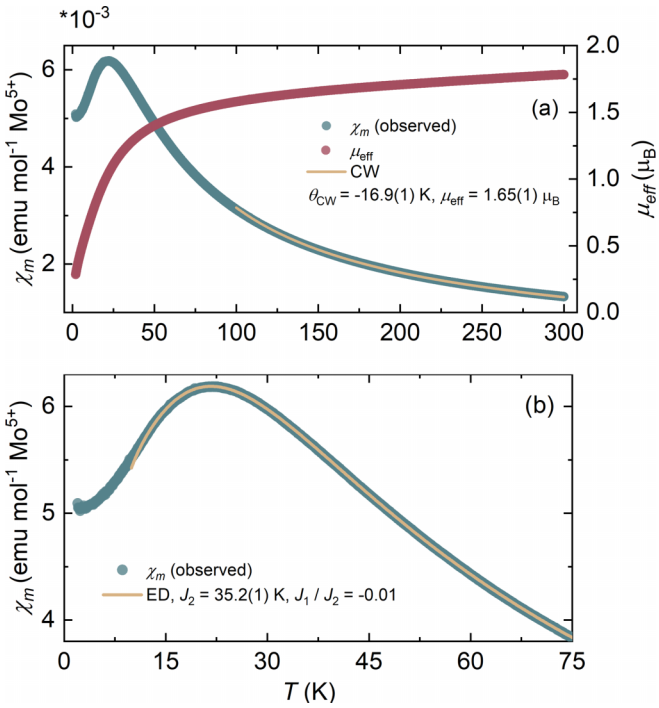

FIG. 3. (a), (left) Temperature-dependent magnetic susceptibility measured in an applied field of $H = 1000$ Oe alongside the (a), (right) calculated effective moment μ_{eff}. A Curie-Weiss fit to the data yields an antiferromagnetic Weiss constant $\theta_{\text{CW}} = -16.9(1)$ K and an effective moment, $\mu_{\text{eff}} = 1.65(1)\mu_{\text{B}}$, reflecting a nearly full spin-only $S = \frac{1}{2}$ moment. (b) Fitting the magnetic susceptibility to an exact diagonalization (ED) calculation of the Heisenberg frustrated chain model with an interchain exchange parameter, J_1, and an intrachain exchange, J_2, yields an effective one-dimensional model with $J_2 = 35.2(1)$ K and $J_1/J_2 = -0.01$.

$N_{\text{A}}\mu_{\text{eff}}^2/3k_{\text{B}}$ and θ_{CW} are the Curie and Weiss constants, respectively, and χ_0 is a temperature-independent background term. Here, the choice for the minimum fitting temperature of 170 K was made based on the stabilization of the extracted parameters beyond this temperature (Fig. S3 of the Supplemental Material [29]). The fit yields the parameters $\theta_{\text{CW}} = -16.9(1)$ K, $C = 0.341(1)$ emu K mol^{-1} ($g = 1.91$), $\mu_{\text{eff}} = 1.65(1)\mu_{\text{B}}$, and $\chi_0 = 2.51 \times 10^{-5}$ emu mol^{-1}, suggesting dominant antiferromagnetic interactions and a moment size close to the full spin-only $S = \frac{1}{2}$ moment of $1.73\mu_{\text{B}}$. This is unlike other Mo^{5+}-containing materials such as Ba_2YMoO_6 [48] and $Lu_2Mo_2O_5N_2$ [49] where a significant orbital contribution is evident by a large deviation of μ_{eff} from its spin-only value. On cooling, the development of short-range correlations is evinced by a broad symmetrical feature, characteristic of quasi-one-dimensional materials centered about 21 K. No features indicative of long-range magnetic order are observed down to 1.8 K.

To approximate the leading magnetic exchanges in $KMoOP_2O_7$, an exact diagonalization calculation has been performed for the $S = \frac{1}{2}$ Heisenberg frustrated chain model using the ALPS software package. Given the similarity between the bonding geometries represented by J_1 and $J_{1'}$, and thus the similarity between the likely superexchange mechanisms, only one interchain exchange is used to approximate both parameters. When fitting χ_m above 15 K, the resulting parameters [$J_2 = 35.2(1)$ K, $J_1/J_2 = -0.01$, $g = 1.96$] are consistent with a leading antiferromagnetic interaction and highlight the one dimensionality of the magnetism in $KMoOP_2O_7$. The minimum fitting temperature here was picked within a region where minimal variation in χ^2 and J_2 is observed. In comparison to the CW model, J_1 could then be estimated using $\theta_{\text{CW}} = -\frac{1}{4}(zJ_1 + z'J_2)$, where z is the number of couplings per site, resulting in $J_1/J_2 \approx -0.04$. While the small $J_1/J_2 = -0.01$ reflects that fitting the magnetic susceptibility cannot produce a reliable estimate of J_1, the resulting model, where interchain exchange plays a minimal role, is confirmed by our electronic structural calculations (Sec. III E) which places $KMoOP_2O_7$ within the one-dimensional limit of the frustrated HAF phase diagram. As a one-dimensional spin chain, this reflects an expected saturation field, $H_{\text{sat}} = 2J_{1\text{D}}/g\mu_{\text{B}}$, of ≈53 T.

C. Specific heat

The temperature dependence of the zero-field molar specific heat, $C_{\text{p,total}}$, is shown in Fig. 4. Considering the insulating behavior expected, the total specific heat, $C_{\text{p,total}}$, can be approximated by the individual contributions of its lattice, $C_{\text{p,phonon}}$, and magnetic, $C_{\text{p,mag}}$, components such that $C_{\text{p,total}} = C_{\text{p,phonon}} + C_{\text{p,mag}}$. To estimate $C_{\text{p,phonon}}$, the phenomenological Debye-Einstein model,

$$C_{\text{p,phonon}}(T) = f_{\text{D}}C_{\text{D}}(\theta_{\text{D}}, T) + \sum_{i=1}^{3} f_{\text{E}_i}C_{\text{E}_i}(\theta_{\text{E}_i}, T), \quad (3)$$

$$C_{\text{D}}(\theta_{\text{D}}, T) = 9nR\left(\frac{T}{\theta_{\text{D}}}\right)^3 \int_0^{\frac{\theta_{\text{D}}}{T}} \frac{x^4 e^x}{(e^x - 1)^2} dx, \quad (4)$$

$$C_E(\theta_E, T) = 3nR\left(\frac{T}{\theta_{\text{E}}}\right)^2 \frac{e^{\theta_{\text{E}}/T}}{(e^{\theta_{\text{E}}/T} - 1)^2}, \quad (5)$$

is used. Here, Eqs. (4) and (5) represent the Debye and Einstein terms and their characteristic temperatures, θ_{D} and θ_{E}, respectively, whereas f_{D} and f_{E} are weighting factors, R is the universal gas constant, and n defines the number of atoms per formula unit. When fitting down to 40 K [Fig. 4(a)], $C_{\text{p,total}}$ is well described by the parameters $\theta_{\text{D}} \simeq 550$ K, $f_{\text{D}} \simeq 0.58$, $\theta_{\text{E}_1} \simeq 90$ K, $f_{\text{E}_1} = 0.11$, $\theta_{\text{E}_2} \simeq 115$ K, $f_{\text{E}_2} = 0.13$, $\theta_{\text{E}_3} \simeq 460$ K, and $f_{\text{E}_3} = 0.18$. Here, four Einstein terms were initially used to reflect the three optical phonons observed in the measured dynamical structure factor [Fig. S6 of the Supplemental Material [29]] plus any additional higher-energy phonon branches. Fitting the lowest-energy phonon, however, proved the fit unstable, and so only three terms were used. By subtracting an extrapolation of the estimated $C_{\text{p,phonon}}$ from $C_{\text{p,total}}$ down to 0.7 K, a broad feature, consistent with an anomaly seen in the Fisher specific heat (Fig. S3 of the Supplemental Material [29]), $d\chi T/dT$, is observed in $C_{\text{p,mag}}$ [Fig. 4(b)]. When using the extracted $J_1 \simeq 35$ K from the exact diagonalization model describing $\chi_{\text{m}}(T)$, we find that the temperature at which this maximum is observed, $T_{\text{max}} \simeq 18$ K, is consistent with the expected $0.48\,J_{1\text{D}} \simeq 18$ K for the $S = \frac{1}{2}$ one-dimensional HAF model [50]. The maximum magnetic

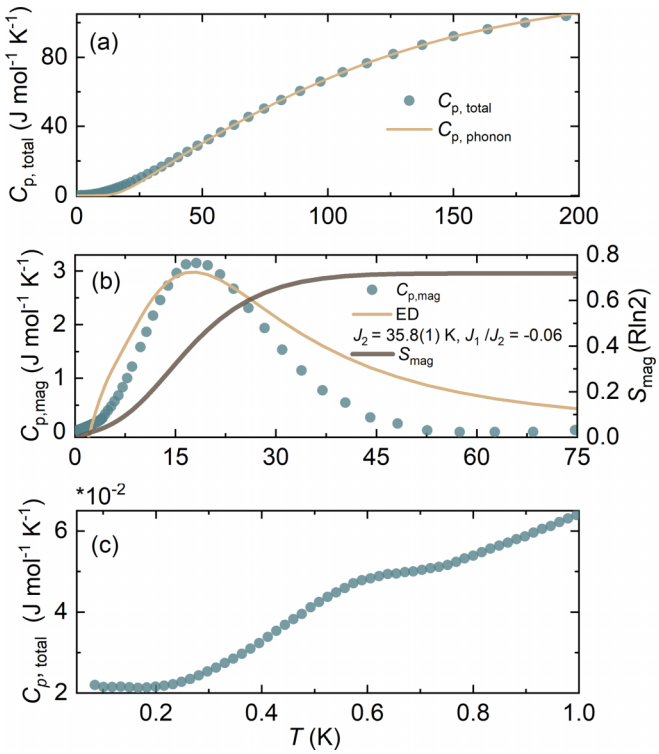

FIG. 4. (a) Temperature dependence of the zero-field total heat-capacity fit to a Debye-Einstein model to approximate the phonon contribution to the specific heat, $C_{\mathrm{p,phonon}}$, yielding $\theta_{\mathrm{D}} \simeq 550$ K, $f_{\mathrm{D}} \simeq 0.58$, $\theta_{\mathrm{E}_1} \simeq 90$ K, $f_{\mathrm{E}_1} = 0.11$, $\theta_{\mathrm{E}_2} \simeq 115$ K, $f_{\mathrm{E}_2} = 0.13$, $\theta_{\mathrm{E}_3} \simeq 460$ K, and $f_{\mathrm{E}_3} = 0.18$. By subtracting $C_{\mathrm{p,phonon}}$ from the total heat capacity (b), (left), the resulting magnetic specific heat, $C_{\mathrm{p,mag}}$, reveals a broad feature centered about 18 K and that can be described by the $S = \frac{1}{2}$ Heisenberg frustrated chain model with an intrachain exchange parameter, $J_2 = 35.8(1)$ K, and an interchain exchange parameter, $J_1/J_2 = -0.06$. This feature is also associated with (b), (right) magnetic entropy release. (c) A broad feature, centered about $T_{\mathrm{N}} = 0.54$ K, is observed in $C_{\mathrm{p,total}}$.

specific heat for this feature, $C^{\mathrm{max}}_{\mathrm{p,mag}} = 3.12$ J mol^{-1} K^{-1}, is also in agreement with the expected $C^{\mathrm{max}}_{\mathrm{p,mag}} = 0.3497 \times R \simeq 2.9$ J mol^{-1} K^{-1} for a uniform $S = \frac{1}{2}$ Heisenberg chain antiferromagnet [51].

To confirm the validity of this model, we then fit $C_{\mathrm{p,mag}}(T)$ to the theoretical curves obtained from the exact diagonalization calculation of the $S = \frac{1}{2}$ Heisenberg frustrated chain model and obtain $J_2 = 35.8(1)$ K and $J_1/J_2 = -0.06$ [Fig. 4(b)]. While the resulting model describes the peak position in $C_{\mathrm{p,mag}}(T)$ and is consistent with minimal frustration, an overestimation of the phonon contribution is evident when compared with the theoretical curve. Indeed, this discrepancy is also observed when estimating the spin entropy release associated with this feature which was calculated as $S_{\mathrm{mag}}(T) = \int_{1\ \mathrm{K}}^{100\ \mathrm{K}} C_{\mathrm{p,mag}}/T$. The resulting $S_{\mathrm{mag}} = 4.15$ J mol^{-1} K^{-1} reflects that only ≈70% of the maximum allowed $R \ln 2$ entropy is released across this feature, which is lower than the theoretical entropy release for the $S = \frac{1}{2}$ HAF model [50]. Additional to the phenomenological nature of the fitting approach, the overestimation of the phonon contribution could also reflect the large thermal motion of the K^+ ions that lie within the relatively large cavities along the a axis.

Below 1 K, the temperature dependence of the total zero-field specific heat reveals a feature centered about $T_{\mathrm{N}} = 0.54$ K. Assuming that it represents the onset of long-range magnetic order, the absence of any significant interchain exchange interactions, $J_\perp < 0.19$ K, is suggested by applying the analytical expression $|J_\perp| \simeq T_{\mathrm{N}}/1.28\sqrt{\ln(5.8J_1/T_{\mathrm{N}})}$ [52] with $T_{\mathrm{N}} < 0.6$ K. An upper limit on the ordered magnetic moment, μ_{ord}, can then be approximated as $\mu_{\mathrm{ord}} < 0.08\ \mu_{\mathrm{B}}$ by using the expression $\mu_{\mathrm{ord}} \simeq 1.017\sqrt{|J_\perp|/J_1}$ [52].

D. Long-range magnetic order

To investigate the nature of the long-range magnetic order, NPD data were collected at 0.05, 1.8, and 20 K on the D20 and WISH diffractometers. While at first glance features consistent with a propagation vector of $\kappa = 0$ can be gleaned from the subtracted data sets, the simulated models for this propagation vector confirm that these features are instead artifacts arising from the subtraction [Fig. S4(a) of the Supplemental Material [29]]. Thus, no features consistent with magnetic Bragg scattering are observed in the subtracted data sets. Instead, if we assume antiferromagnetic ordering along the chain direction, $\kappa = (\frac{1}{2}00)$, as justified by the crystal structure (Sec. III A) and the electronic structure (Sec. III E), an upper limit of $\mu_{\mathrm{ord}} < 0.15\ \mu_{\mathrm{B}}$ can be estimated for all moment directions at 0.05 K [Fig. S4(b)]. This strong suppression of the ordered moment is consistent with $KMoOP_2O_7$ residing close to the pure one-dimensional-chain limit. Indeed, such a reduction is characteristic of the $S = \frac{1}{2}$ antiferromagnetic Heisenberg chain spin model and is generally observed across its various material realizations [53,54].

E. Microscopic magnetic model

To better understand the Heisenberg one-dimensional character of the magnetic correlations observed thus far, we now turn to the electronic structure. In the absence of correlations, the GGA band structure of $KMoOP_2O_7$ is metallic. The bands between −0.5 and 4 eV have predominantly Mo $4d$ origin [Fig. S5 [29]]. The apparent Heisenberg nature of the spins can be understood as the structure of $KMoOP_2O_7$ features strongly distorted MoO_6 octahedra. Here, the short apical Mo–O bond splits the t_{2g} states into the lower-lying d_{xy} orbital and higher-lying, nearly degenerate d_{yz} and d_{xz} orbitals. This raises the orbital degeneracy of $4d^1$ Mo^{5+} and leads to purely Heisenberg spins. This is similar to the crystal-field splitting of V^{4+} that also forms short apical bonds within the VO_6 octahedra as in α-$KVOPO_4$ [46]. Orbital energies for $KMoOP_2O_7$ determined from the tight-binding fit of the band structure are $\epsilon_{xy} = 0.02$ eV, $\epsilon_{yz} = 0.98$ eV, $\epsilon_{xz} = 1.03$ eV, $\epsilon_{x^2-y^2} = 3.09$ eV, and $\epsilon_{3z^2-r^2} = 4.50$ eV. The crystal-field splittings are about twice as large as in the case of V^{4+} in an oxide crystal field [40,55], reflecting the larger spatial extent of $4d$ orbitals compared with $3d$. The exchange couplings obtained from Eq. (2) and from DFT + U calculations are listed in Table I. The leading interaction J_2 runs along the a direction and connects the Mo^{5+} ions into linear spin chains. The mechanism of this interaction is the Mo-O-P-O-Mo superexchange

TABLE I. Exchange couplings in $KMoOP_2O_7$. The values of J_{ij}^{AFM} and J_{ij}^{FM} are derived from the Kugel-Khomskii model (2) and show the relative contributions of different superexchange mechanisms. Total exchange couplings J_{ij} are obtained by the DFT + U mapping analysis and may be different from J_{ij}^{AFM} and J_{ij}^{FM}.

	$d_{Mo\text{-}Mo}$ (Å)	J_{ij}^{AFM} (K)	J_{ij}^{FM} (K)	J_{ij} (K)
J_2	5.085(1)	71	−8	34
J_1	5.360(5)	0	−1.6	−1.4
J_1'	5.401(5)	0	−1.4	−1.8
J_b	6.180(1)	0	−0.3	−0.4

via two equivalent bridges formed by the PO_4 tetrahedra. A similar interaction mechanism is known for $(VO)_2P_2O_7$ [56], $VOPO_4 \cdot 0.5H_2O$ [57], and other V^{4+} phosphates, where the double PO_4 bridges cause magnetic interactions on the order of 100 K. The interaction in $KMoOP_2O_7$ is much weaker, probably due to the lateral displacement of the octahedra, which is known to be unfavorable for superexchange [58] and indeed restricts the overlap of oxygen p orbitals along the edge of the tetrahedron (Fig. 5). The main interchain interactions J_1 and J_1' are weakly ferromagnetic and zigzag in nature. Residual and nonfrustrated coupling J_b connects the chains along the b direction and is similarly ferromagnetic.

F. Inelastic neutron scattering

Having determined the source of the observed one-dimensional magnetic correlations, we now return to the magnetic Hamiltonian of the system. The experimental dynamical structure factor, $S(Q, E = \hbar\omega)$, measured at 1.8 K, is shown in Fig. S6(a) [29]. At first glance, spurious scattering arising from the sample environment is observed below 2.5 meV at low angles. To correct for this background, we subtract the dynamical structure factor of the diamagnetic analog [Fig. S6(c) [29]], $KNbOP_2O_7$, from the experimental data of $KMoOP_2O_7$. This is justified by the similar phonon spectra of the materials. Here, a scaling factor of 1.1 was used to provide the cleanest subtraction. As seen in the resulting spectrum [Fig. 6(a)], however, remnants of this spurious scattering, alongside a phonon branch centered about 5.5 meV and peaked around 3 Å^{-1}, cannot be fully corrected for. As such, our analysis is confined within the $E > 2.5$ meV and $Q < 3$ Å^{-1} regions of the spectrum which are least contaminated by these features.

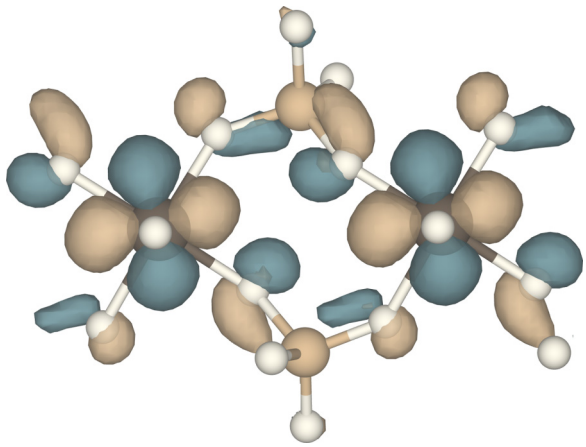

FIG. 5. Mo d_{xy}-based Wannier functions showing the orbital overlap for the J_1 superexchange pathway.

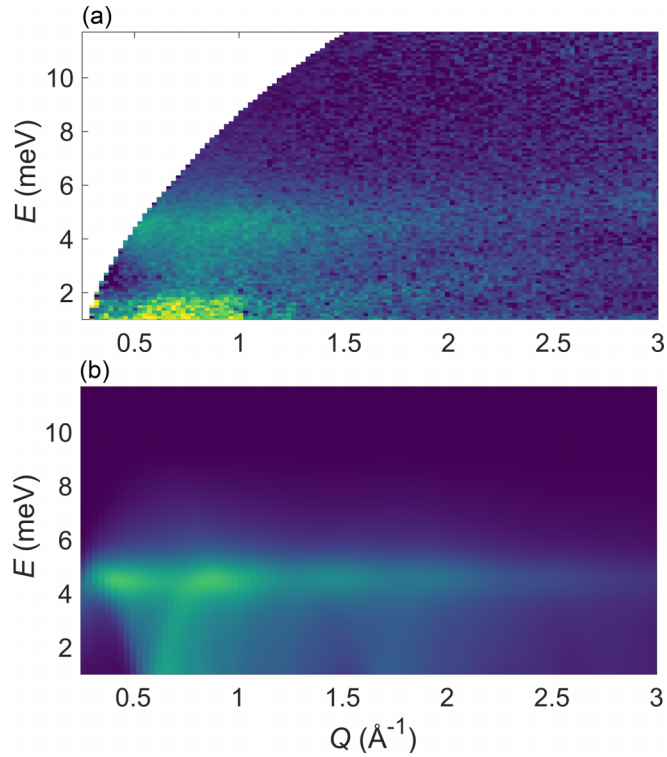

FIG. 6. (a) Phonon-subtracted experimental dynamical structure factor $S(Q, E)$ measured at 1.8 K using an incident energy of $E_i = 14.2$ meV on the IN5 spectrometer. The spurious intensity below 2.5 meV is associated with scattering from the sample environment. (b) Powder-averaged and E-resolution convoluted $S(Q, E)_{2+4}^{calc}$ calculated for $J_1 = 34.4$ K $J_2 = -1.8$ K.

When considering the background-subtracted $S(Q, E)$ [Fig. 6(a)], an accumulation of inelastic spectral weight in a broad feature, peaked about 4.5 meV [Fig. 7(a)], is clearly observed. Alongside the one-dimensional dynamics inferred from the analysis thus far, the sharp onset of magnetic scattering above 0.5 Å^{-1} [Figs. 7(b) and 7(c)] could be associated with powder averaged one-dimensional excitations. Indeed, to a first approximation, the leading exchange parameter, $J_2 = 3.02(1)$ meV, extracted from the exact diagonalization fits to $\chi_m(T)$ and $C_{p,mag}(T)$, coincides with the expected upper limit of the lower bound of the two-spinon continuum, $\pi J_{1D}/2 \simeq 4.7$ meV.

To quantify the leading magnetic exchanges in $KMoOP_2O_7$, a random-phase approximation (RPA)-style approach [36] using the dynamical structure factor of the two- and four-spinon continuum, $S(Q, E)_{2+4}^{calc}$ [35], was applied for the Hamiltonian

$$\mathcal{H} = J_2 \sum_{n,n+1}^{N} S_n \cdot S_{n+1} + J_1 \sum_{n,n+2}^{N} S_n \cdot S_{n+2}. \quad (6)$$

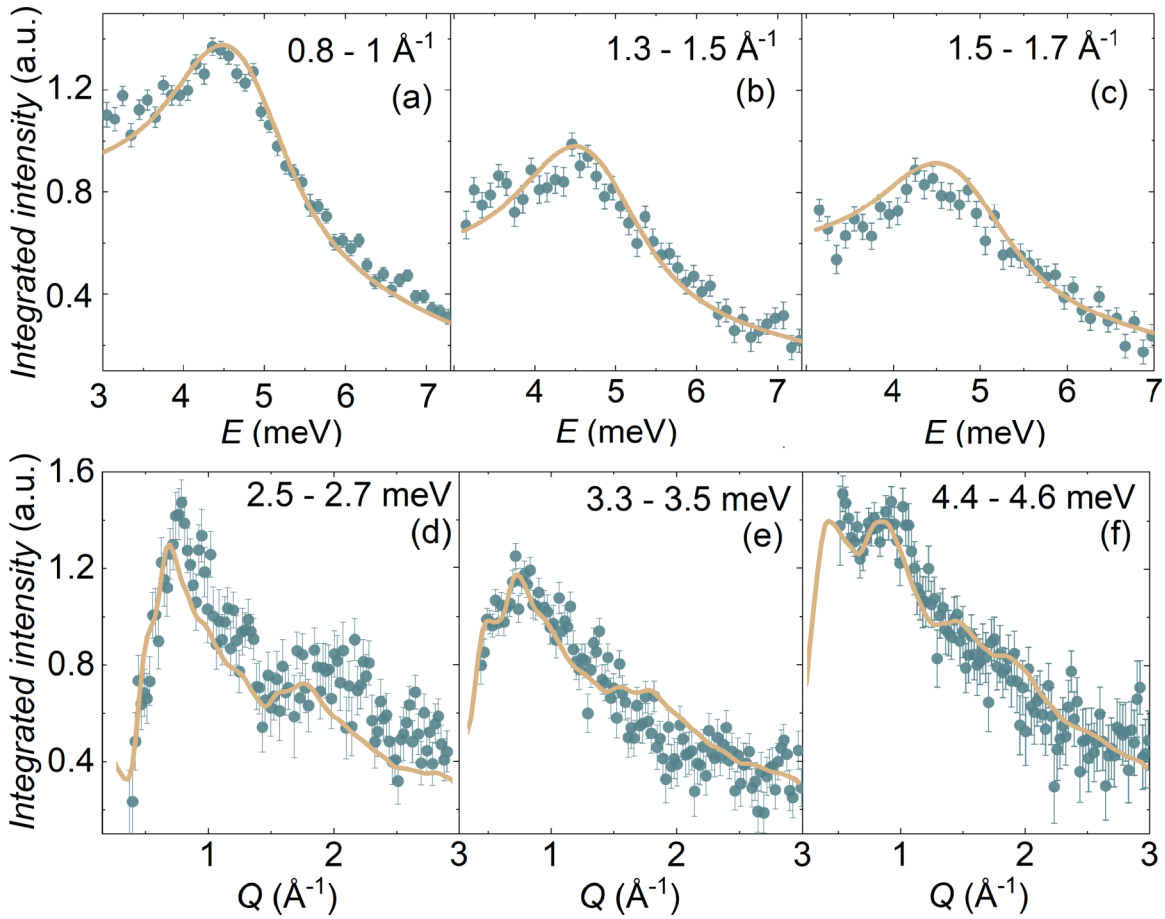

FIG. 7. (a)–(c) ΔE- and (d)–(f) Q-integrated cuts (closed circles) fit to the $S(Q,E)^{\text{calc}}_{2+4}$ calculated as described in the text. The resulting model yields $J_2 = 34.4$ K and $J_1 = -1.8$ K.

To optimize the model, four ΔE cuts, integrated over $\delta Q = 0.1$ Å^{-1} and centered around 0.9, 1.1, 1.4, and 1.6 Å^{-1}, were used. The calculated model, powder-averaged and convoluted to the E-dependent resolution, was then fit to the experimental data using a particle swarm optimization algorithm. While the resulting model parameters were consistently within the range of 2.93 to 2.96 meV and 0.12 to 0.16 meV for J_2 and $|(J_1)|$, respectively, the sign of the latter was undetermined by the fitting. By considering the effect of the sign of J_1 on multiple ΔQ cuts, integrated over $\delta E = 0.2$ meV, however, the best-fit model was found for $J_2 = 34.4$ K (2.95 meV) and $J_1 = -1.8$ K [-0.16 meV, Figs. 7(a)–7(f)]. Indeed, although the redistribution of spectral weight resulting from J_1 is expected to be most pronounced within contaminated regions of $S(Q,E)$, a characteristic narrowing of the peaks in ΔQ was consistent among solutions with ferromagnetic J_1 (Fig. S7). Furthermore, the resulting model is consistent with both models obtained through the DFT + U calculations (Table I) and the exact diagonalization fits to $\chi_{\text{m}}(T)$ and $C_{\text{p,mag}}(T)$. Extracting a more conclusive estimate of J_1 will require analysis of a dynamical structure factor measured for a single-crystalline sample. Regardless of the sign of J_1, however, the resulting model is widely consistent with $KMoOP_2O_7$ falling within the one-dimensional limit of the HAF phase diagram with $|J_1|/J_2 < 0.05$. Finally, it should be noted that uniform Dzyaloshinskii–Moriya (DM) interactions are allowed along the chain direction. While it cannot be conclusively disregarded, no signs of incommensurate magnetic order, which is expected even for a small DM interaction [59,60], could be observed in any data set.

IV. CONCLUSION

In summary, we have presented a comprehensive investigation of the structural and magnetic properties of the one-dimensional $S = \frac{1}{2}$ Mo^{5+} system, $KMoOP_2O_7$. Using powder neutron diffraction, the previously published structure of $KMoOP_2O_7$ has been verified down to 50 mK. Analysis of magnetic susceptibility data revealed one-dimensional magnetic correlations that are consistent with the observed magnetic specific heat. While a broad feature is observed at $T_{\text{N}} = 0.54$ K in the temperature dependence of the specific heat, no magnetic Bragg scattering is observed down to 0.05 K, which we ascribe to the strong one-dimensional character of the correlations in $KMoOP_2O_7$. This result is confirmed by our *ab initio* calculations which reveal an active d_{xy} magnetic orbital, resulting from distortions to the Mo^{5+}-containing octahedra, favoring superexchange along the chain direction. We finally determine the spin magnetic Hamiltonian through analysis of powder inelastic neutron-scattering data resulting in a model that is broadly consistent with all experimental results. We thus propose $KMoOP_2O_7$ as a near ideal

realization of the $S = \frac{1}{2}$ Heisenberg one-dimensional chain antiferromagnet model.

When considering other $S = \frac{1}{2}$ Heisenberg quasi-one-dimensional antiferromagnet materials that are amenable to frustration, the magnetic ground state of $KMoOP_2O_7$ is reminiscent to that seen in other materials falling on the one-dimensional limit such as in $CuSe_2O_5$ [61] and Sr_2CuO_3 [62,63]. The one-dimensional character of the magnetic correlations in $KMoOP_2O_7$ also highlights the significance of the crystalline electric field in determining the effective magnetic ground state. It could then be interesting to examine the role of the monovalent ion site, A, in $AMoOP_2O_7$, in tuning the energy scales in the system, especially given the slight structural variations for $A =$ Na [26], Cs [27]. Investigating the effect of the superexchange mediating ion on the magnetic properties of the system could also prove fruitful by studying $KMoV_2O_8$ as the analogous compounds, AMP_2O_8 ($A =$ Tl, K, Rb, Cs, $M =$ Nb, Ta), exist [64]. Finally, the roles of the spin and orbital degrees of freedom could be explored in the $5d$ $S = \frac{1}{2}$ W^{5+} analog, $KWOP_2O_7$ [65].

ACKNOWLEDGMENTS

Provision of a Ph.D. studentship to A.H.A. by the University of Birmingham and the Science and Technology Facilities Council (STFC) is gratefully acknowledged. The authors are also grateful to the STFC for access to neutron beamtime at ISIS, to Dr. P. Manuel (WISH), and thank Dr. G. Stenning for aiding with magnetic susceptibility and specific-heat measurements at the Material Characterization Laboratory at ISIS. The Institut Laue-Langevin (ILL) is acknowledged for beam time allocation under the experiment codes 5-31-2822 [30] and EASY-844 [34] for the D20 and IN5 experiments, respectively.

[1] C. Nayak, S. H. Simon, A. Stern, M. Freedman, and S. Das Sarma, Rev. Mod. Phys. **80**, 1083 (2008).
[2] A. Kitaev, Ann. Phys. (NY) **303**, 2 (2003).
[3] V. Lahtinen and J. Pachos, SciPost Phys. **3**, 021 (2017).
[4] C. Broholm, R. J. Cava, S. A. Kivelson, D. G. Nocera, M. R. Norman, and T. Senthil, Science **367**, eaay0668 (2020).
[5] L. Savary and L. Balents, Rep. Prog. Phys. **80**, 016502 (2017).
[6] L. Clark and A. H. Abdeldaim, Annu. Rev. Mater. Res. **51**, 495 (2021).
[7] C. Castelnovo, R. Moessner, and S. L. Sondhi, Annu. Rev. Condens. Matter Phys. **3**, 35 (2012).
[8] M. Hermanns, I. Kimchi, and J. Knolle, Annu. Rev. Condens. Matter Phys. **9**, 17 (2018).
[9] D. E. Feldman and B. I. Halperin, Rep. Prog. Phys. **84**, 076501 (2021).
[10] H. Bethe, Eur. Phys. J. A **71**, 205 (1931).
[11] L. Hulthén, Über das Austauschproblem eines Kristalles, Ph.D. thesis, German, 1938, https://www.diva-portal.org/smash/record.jsf?pid=diva2%3A491955&dswid=-3188.
[12] D. A. Tennant, T. G. Perring, R. A. Cowley, and S. E. Nagler, Phys. Rev. Lett. **70**, 4003 (1993).
[13] M. Mourigal, M. Enderle, A. Klöpperpieper, J.-S. Caux, A. Stunault, and H. M. Rønnow, Nat. Phys. **9**, 435 (2013).
[14] R. Coldea, D. A. Tennant, E. M. Wheeler, E. Wawrzynska, D. Prabhakaran, M. Telling, K. Habicht, P. Smeibidl, and K. Kiefer, Science **327**, 177 (2010).
[15] Z. Wang, M. Schmidt, A. K. Bera, A. T. M. N. Islam, B. Lake, A. Loidl, and J. Deisenhofer, Phys. Rev. B **91**, 140404(R) (2015).
[16] A. Vasiliev, O. Volkova, E. Zvereva, and M. Markina, npj Quantum Mater. **3**, 18 (2018).
[17] F. D. M. Haldane, Phys. Rev. B **25**, 4925 (1982).
[18] K. Okamoto and K. Nomura, Phys. Lett. A **169**, 433 (1992).
[19] S. Eggert, Phys. Rev. B **54**, R9612 (1996).
[20] M. Enderle, C. Mukherjee, B. Fåk, R. K. Kremer, J.-M. Broto, H. Rosner, S.-L. Drechsler, J. Richter, J. Malek, A. Prokofiev, W. Assmus, S. Pujol, J.-L. Raggazzoni, H. Rakoto, M. Rheinstädter, and H. M. Rønnow, Europhys. Lett. **70**, 237 (2005).
[21] S. E. Dutton, M. Kumar, M. Mourigal, Z. G. Soos, J.-J. Wen, C. L. Broholm, N. H. Andersen, Q. Huang, M. Zbiri, R. Toft-Petersen, and R. J. Cava, Phys. Rev. Lett. **108**, 187206 (2012).
[22] G. J. Nilsen, H. M. Rønnow, A. M. Läuchli, F. P. A. Fabbiani, J. Sanchez-Benitez, K. V. Kamenev, and A. Harrison, Chem. Mater. **20**, 8 (2008).
[23] D. Kasinathan, K. Koepernik, O. Janson, G. J. Nilsen, J. O. Piatek, H. M. Rønnow, and H. Rosner, Phys. Rev. B **88**, 224410 (2013).
[24] C. Gueho, M. M. Borel, A. Grandin, A. Leclaire, and B. Raveau, Z. Anorg. Allg. Chem. **615**, 104 (1992).
[25] E. Canadell, J. Provost, A. Guesdon, M. M. Borel, and A. Leclaire, Chem. Mater. **9**, 68 (1997).
[26] S. Ledain, A. Leclaire, M. M. Borel, J. Provost, and B. Raveau, J. Solid State Chem. **124**, 24 (1996).
[27] A. Guesdon, M. M. Borel, A. Leclaire, A. Grandin, and B. Raveau, J. Solid State Chem. **108**, 46 (1994).
[28] K. Momma and F. Izumi, J. Appl. Crystallogr. **41**, 653 (2008).
[29] See Supplemental Material at http://link.aps.org/supplemental/10.1103/PhysRevB.107.014415 for synthesis and structural confirmation of $KNbOP_2O_7$, temperature dependence of the lattice parameters of $KMoOP_2O_7$, GGA density of states, and as-measured inelastic neutron-scattering spectra of both compounds.
[30] A. H. Abdeldaim, L. Clark, G. J. Nilsen, and C. Ritter, https://doi.ill.fr/10.5291/ILL-DATA.5-31-2886 (2021).
[31] B. H. Toby, J. Appl. Crystallogr. **34**, 210 (2001).
[32] N. Qureshi, J. Appl. Crystallogr. **52**, 175 (2019).
[33] H. Ishikawa, N. Nakamura, M. Yoshida, M. Takigawa, P. Babkevich, N. Qureshi, H. M. Rønnow, T. Yajima, and Z. Hiroi, Phys. Rev. B **95**, 064408 (2017).
[34] A. H. Abdeldaim, L. Clark, G. J. Nilsen, and J. Ollivier, https://doi.ill.fr/10.5291/ILL-DATA.EASY-844 (2021).
[35] J.-S. Caux and R. Hagemans, J. Stat. Mech.: Theory Exp. (2006) P12013.
[36] M. Kohno, O. A. Starykh, and L. Balents, Nat. Phys. **3**, 790 (2007).
[37] K. Koepernik and H. Eschrig, Phys. Rev. B **59**, 1743 (1999).

[38] J. P. Perdew, K. Burke, and M. Ernzerhof, Phys. Rev. Lett. **77**, 3865 (1996).
[39] V. V. Mazurenko, F. Mila, and V. I. Anisimov, Phys. Rev. B **73**, 014418 (2006).
[40] A. A. Tsirlin, O. Janson, and H. Rosner, Phys. Rev. B **84**, 144429 (2011).
[41] H. J. Xiang, E. J. Kan, S.-H. Wei, M.-H. Whangbo, and X. G. Gong, Phys. Rev. B **84**, 224429 (2011).
[42] A. A. Tsirlin, Phys. Rev. B **89**, 014405 (2014).
[43] Y. Iqbal, T. Müller, K. Riedl, J. Reuther, S. Rachel, R. Valentí, M. J. P. Gingras, R. Thomale, and H. O. Jeschke, Phys. Rev. Mater. **1**, 071201(R) (2017).
[44] J. Hembacher, D. I. Badrtdinov, L. Ding, Z. Sobczak, C. Ritter, V. V. Mazurenko, and A. A. Tsirlin, Phys. Rev. B **98**, 094406 (2018).
[45] A. H. Abdeldaim, D. I. Badrtdinov, A. S. Gibbs, P. Manuel, H. C. Walker, M. D. Le, C. H. Wu, D. Wardecki, S.-G. Eriksson, Y. O. Kvashnin, A. A. Tsirlin, and G. J. Nilsen, Phys. Rev. B **100**, 214427 (2019).
[46] P. K. Mukharjee, K. Somesh, K. M. Ranjith, M. Baenitz, Y. Skourski, D. T. Adroja, D. Khalyavin, A. A. Tsirlin, and R. Nath, Phys. Rev. B **104**, 224409 (2021).
[47] D. Urushihara, S. Kawaguchi, K. Fukuda, and T. Asaka, IUCrJ **7**, 656 (2020).
[48] M. A. de Vries, A. C. Mclaughlin, and J.-W. G. Bos, Phys. Rev. Lett. **104**, 177202 (2010).
[49] L. Clark, G. J. Nilsen, E. Kermarrec, G. Ehlers, K. S. Knight, A. Harrison, J. P. Attfield, and B. D. Gaulin, Phys. Rev. Lett. **113**, 117201 (2014).
[50] D. C. Johnston, R. K. Kremer, M. Troyer, X. Wang, A. Klümper, S. L. Bud'ko, A. F. Panchula, and P. C. Canfield, Phys. Rev. B **61**, 9558 (2000).
[51] B. Bernu and G. Misguich, Phys. Rev. B **63**, 134409 (2001).
[52] H. J. Schulz, Phys. Rev. Lett. **77**, 2790 (1996).
[53] G. J. Nilsen, A. Raja, A. A. Tsirlin, H. Mutka, D. Kasinathan, C. Ritter, and H. M. Rønnow, New J. Phys. **17**, 113035 (2015).
[54] A. A. Belik, S. Uji, T. Terashima, and E. Takayama-Muromachi, J. Solid State Chem. **178**, 3461 (2005).
[55] A. A. Tsirlin, R. Nath, J. Sichelschmidt, Y. Skourski, C. Geibel, and H. Rosner, Phys. Rev. B **83**, 144412 (2011).
[56] A. W. Garrett, S. E. Nagler, D. A. Tennant, B. C. Sales, and T. Barnes, Phys. Rev. Lett. **79**, 745 (1997).
[57] D. A. Tennant, S. E. Nagler, A. W. Garrett, T. Barnes, and C. C. Torardi, Phys. Rev. Lett. **78**, 4998 (1997).
[58] M. Roca, P. Amorós, J. Cano, M. D. Marcos, J. Alamo, A. Beltrán-Porter, and D. Beltrán-Porter, Inorg. Chem. (Washington, DC, U.S.) **37**, 3167 (1998).
[59] M. Hälg, W. E. A. Lorenz, K. Y. Povarov, M. Månsson, Y. Skourski, and A. Zheludev, Phys. Rev. B **90**, 174413 (2014).
[60] R.-B. Wang, A. Keselman, and O. A. Starykh, Phys. Rev. B **105**, 184429 (2022).
[61] O. Janson, W. Schnelle, M. Schmidt, Y. Prots, S.-L. Drechsler, S. K. Filatov, and H. Rosner, New J. Phys. **11**, 113034 (2009).
[62] K. M. Kojima, Y. Fudamoto, M. Larkin, G. M. Luke, J. Merrin, B. Nachumi, Y. J. Uemura, N. Motoyama, H. Eisaki, S. Uchida, K. Yamada, Y. Endoh, S. Hosoya, B. J. Sternlieb, and G. Shirane, Phys. Rev. Lett. **78**, 1787 (1997).
[63] H. Rosner, H. Eschrig, R. Hayn, S.-L. Drechsler, and J. Málek, Phys. Rev. B **56**, 3402 (1997).
[64] A. K. Paidi, R. N. Devi, and K. Vidyasagar, Dalton Trans. **44**, 17399 (2015).
[65] A. Leclaire, J. Chardon, and B. Raveau, J. Mater. Chem. **11**, 846 (2001).